Supplementary Information

Real-time ultra-sensitive detection of SARS-CoV-2 by quasi-freestanding epitaxial graphene-based biosensor

Soaram Kim[*†]*, Heeju Ryu*[†]*, Sheldon Tai, Michael Pedowitz, John Robertson Rzasa, Daniel J. Pennachio, Jenifer R. Hajzus, Donald K. Milton, Rachael Myers-Ward, Kevin M. Daniels*[*]

Dr. S. Kim, M. Pedowitz, Prof. K.M. Daniels
Department of Electrical and Computer Engineering, University of Maryland, College Park, MD 20742, USA
Institute for Research in Electronics and Applied Physics, University of Maryland, College Park, MD 20742, USA
E-mail: soaramk@umd.edu; danielkm@umd.edu

Dr. H. Ryu
Vaccine and Infectious Diseases Division, Fred Hutchinson Cancer Research Center, Seattle, WA, 98109 USA

Prof. S. Tai, Prof. D.K. Milton
Maryland Institute for Applied Environmental Health, University of Maryland School of Public Health, College Park, MD 20742, USA

Dr. J.R. Rzasa
Fischell Department of Bioengineering, University of Maryland, College Park, MD 20742, USA

Dr. D. J. Pennachio, Dr. J. R. Hajzus, Dr. R. Myers-Ward,
US Naval Research Laboratory, Washington, DC 23075, USA

[†]These authors contributed equally to this work.

Atomic Force Microscopy (AFM) Analysis:

AFM images were taken using an Asylum Cypher ES environmental AFM operating in tapping mode using Tap3000GD cantilevers. The resulting images were then analyzed using Gwyddion (v.2.58).
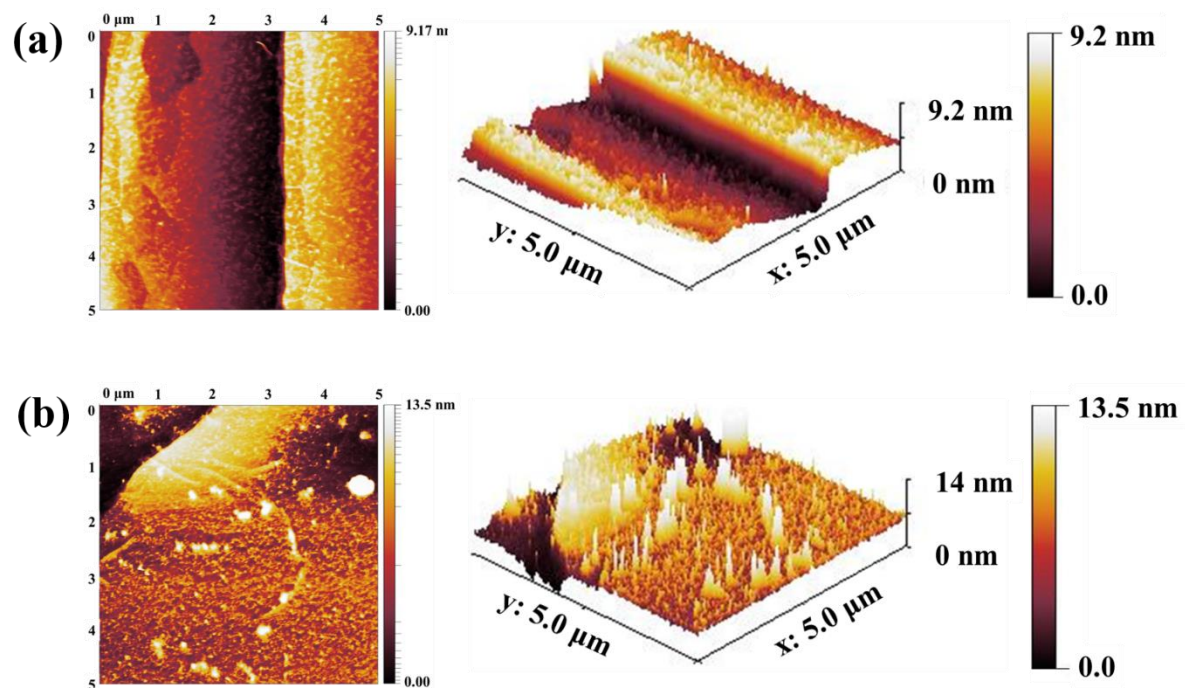

Figure S1 Atomic force microscopy images of (a) quasi-freestanding bilayer epitaxial graphene (EG) on silicon carbide (SiC) and (b) crosslinker on EG/SiC. The root-mean-square (RMS) roughness of EG and crosslinker are 0.7 nm and 0.8 nm, respectively.

X-ray Photoelectron Spectroscopy (XPS) Analysis:

The X-ray photoelectron spectroscopy (XPS) measurements were collected in a Kratos Axis 165 X-ray photoelectron spectrometer operating in hybrid mode using monochromatized Al Kα radiation ($\hbar\omega=1486.7eV$) at an anode power of 280 W. The survey spectra and high-resolution spectra were collected at pass energies of 160 eV and 40 eV, respectively, under a base pressure of 5×10^{-8} torr. The resulting binding energies were referenced to the Si-C bond in the C1s at 282.6 eV [1] to account for surface charging effects. The high-resolution spectra were then deconvoluted using 30 percent Lorentzian Gaussian-Lorentzian line shapes and a Shirley background apart from the asymmetric C-C sp^2 bonding. Finally, the C-C sp^2 bond was fit using an asymmetric pseudo-Voight line shape, equivalent to the traditional Doniach Sunjic line shape found in the literature, with the advantage of having a finite area for analysis [2].

Figure S2(a)-(d) presents the XPS results from the EG. The C1s region in the EG is well fitted with three components, two Gaussian-Lorentzian peaks at 282.61 and 291 eV, and an asymmetric peak at 284.3 eV corresponding to the Si-C bonding, the $\pi-\pi^*$ shake-up peak, and the C-C sp^2 bonding, respectively, as shown in Fig. S2(b) [1,3,4]. The lack of sp^3 hybridized carbon-bonding and carbon-oxygen functional groups indicates that the graphene contains minimal defects in its pristine state. To further verify the graphene quality, O1s and N1s regions were analyzed as shown in Fig. S2(c) and (d). In the O1s region, there is a Gaussian-Lorentzian peak at 532.8 eV, corresponding to the O=C bond [4] with a very low intensity (<1% of the total spectral area). This corroborates that the epitaxial graphene contains minimal defects because it is small relative to the number of carbon atoms in the graphene layer. Additionally, there are no meaningful peaks in the N1s region, indicating no nitrogen is present in the initial EG surface.
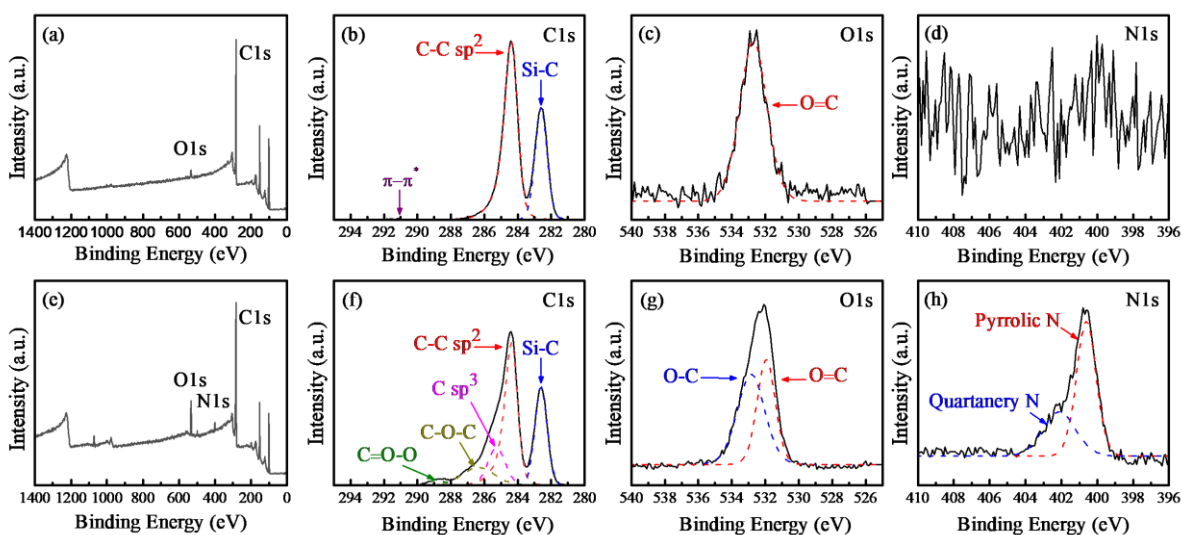
Figure S2 XPS characterizations of (a)-(d) pure EG on SiC and (e)-(h) antibody/crosslinker prepared on EG/SiC.

Figure S2(e)-(h) shows the XPS results from the SARS-CoV-2 S1 protein antibody/crosslinker on EG/SiC. The C1s region is well fitted with five components, four Gaussian-Lorentzian peaks at 282.61, 285.3, 286.4, and 288.9 eV, as well as an asymmetric peak at 284.3 eV, corresponding to the Si-C bonding, C sp^3 bonding, epoxy (C-O-C) groups, carboxyl (O-C=O) groups, and C-C sp^2 bonding, respectively, as shown in Fig. S2(f) [1,3,4]. The presence of these additional C1s components indicates that the SARS-CoV-2 S1 spike protein antibody/crosslinker structure has been successfully immobilized onto the EG structure. The presence of a C sp^3 bonding component to the C1s spectra indicates the formation of defects within the graphene layers; however, Raman analysis (Figure S3) indicates the crosslinker (i.e., poly-L-lysine) bonds to the graphene through a non-covalent cation-π bonding mechanism. This causes us to conclude that the additional components of the C1s spectra are due to features within the SARS-CoV-2 S1 spike protein antibody/crosslinker structure as opposed to defects to the underlying EG layer. Further analysis of the O1s and N1s regions also indicates the presence of additional atomic species compared to pristine EG, which further corroborates that the SARS-CoV-2 S1 spike protein

antibody/crosslinker structure has been successfully immobilized in the EG surface. In the O1s region, there are two Gaussian-Lorentzian peaks at 532 and 532.9 eV that correspond to O-C and O=C, respectively, as shown in Fig. S2(g) [4,5]. In the N1s region, there are two Gaussian-Lorentzian peaks, in contrast to EG, at 400.6 and 402.1 eV, corresponding to pyrrolic nitrogen groups and quaternary nitrogen groups, respectively, as shown Fig. S2(h) [5].

Raman Analysis:

Raman spectroscopy was conducted using a Horiba LABRAM ARAMIS system using a 532nm laser source with laser power of 14.7mW. The spectra were taken using a 600 grove/mm grating for five accumulation of 10 seconds. After the spectra were captured, they were then processed by subtracting a known SiC background and fitted using Lorentzian line shapes.

Figure S3 presents the typical Raman spectra of (a) EG on SiC and the subsequent evolution of the Raman spectra through the bonding of (b) the crosslinker and (c) SARS-CoV-2 S1 spike protein antibody on EG/SiC. Figure S3(d) presents the Raman spectra of the crosslinker/EG/SiC structure after cleaning in NaCl solution (1 M) to remove the SARS-CoV-2 S1 spike protein antibody. From the Raman spectra of the EG on SiC, the D peak is not visible above the background noise, which indicates the synthesized graphene has a very low defect density and is dominated by sp^2 bonded carbons (Fig. S3(a)). After bonding the crosslinker to the EG/SiC surface, we observed a redshift of G peak by 6 cm^{-1} from 1594.8cm^{-1} to 1588.8cm^{-1} while the D peak remained below the background noise (Fig. S3(b)). The position of the G peak is related to the carrier density of the graphene layer [6-8]. The redshift of the G peak in the Raman results shows that the bonding of the crosslinker depleted the charge carriers of the epitaxial graphene layer toward the Dirac point since graphene is p-type [1], i.e., the upward movement of the Fermi level. This is consistent with non-covalent cation-π bonding between the sp^2 carbons in graphene and protonated amine groups within crosslinker structure, wherein the incorporation of cations into the π system causes a transfer of electrons into the graphene structure [9,10]. This is corroborated by the lack of a visible defect peak, indicating a non-covalent bonding mechanism between the EG and the crosslinker [10].
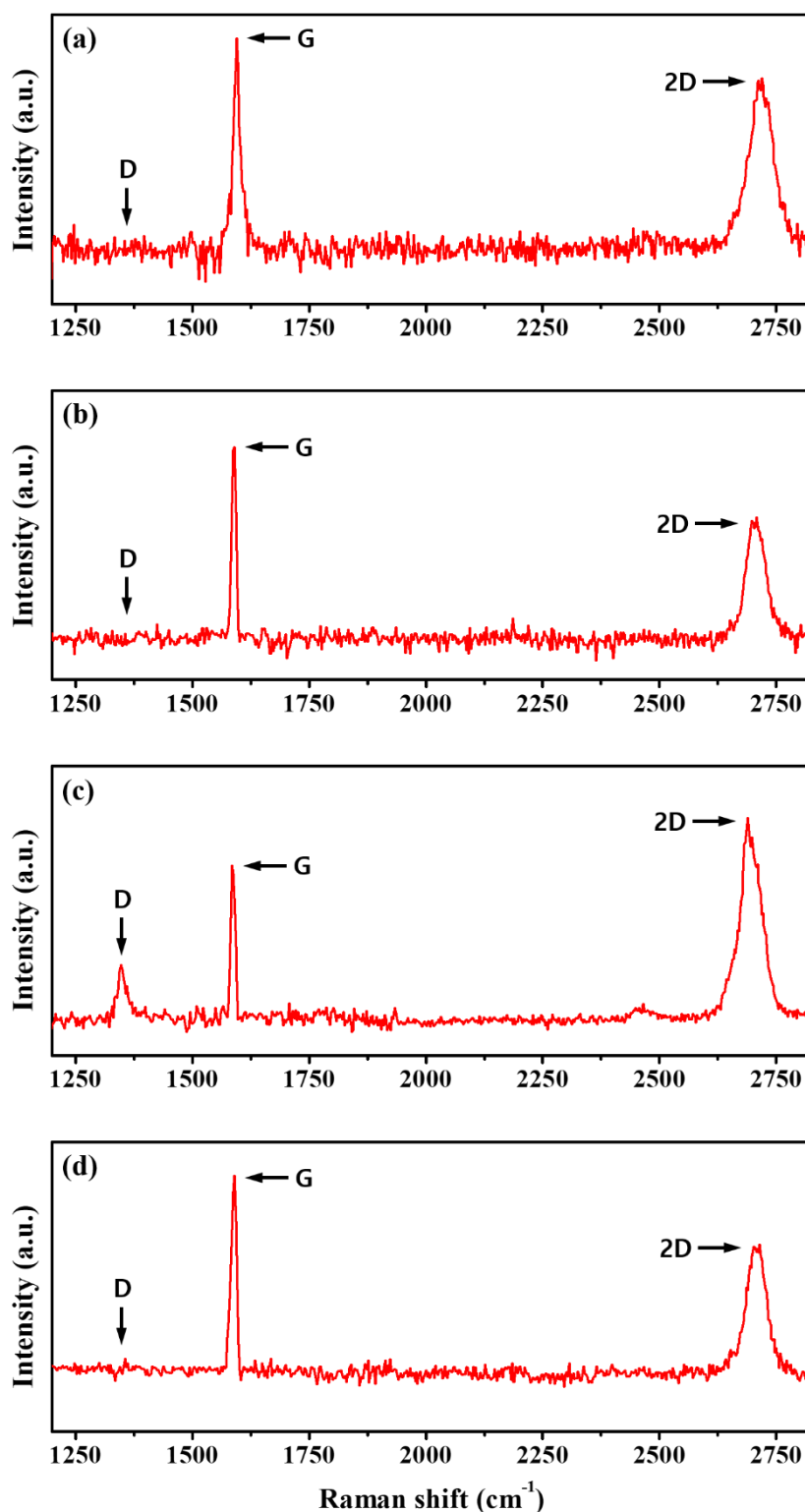
Figure S3 (a) Typical Raman spectra of EG on SiC substrate confirming nominally defect-free graphene. (b) Raman spectra of the crosslinker prepared on EG/SiC showing a 6 cm^{-1} redshift of the G peak compared to pure EG on SiC substrate. (c) Raman spectra of the antibody/crosslinker/EG/SiC structure displaying a significant defect peak and additional 2.5cm^{-1} redshift of the G peak. (d) Raman spectra after sample cleaning with NaCl solution (1 M) to remove the bonded antibody, showing a complete recovery of the D peak, and a 2.5cm^{-1} blueshift of the G peak, returning to the spectra seen for the crosslinker/EG/SiC substrate. The SiC substrate contributions were subtracted in the Raman results.

After the subsequent bonding of the antibody to the crosslinker/EG/SiC, we observed an additional 2.5 cm^{-1} redshift of the G peak and the formation of a strong D peak at 1349.3 cm^{-1} (Fig S3(c)). The redshift of the G peak indicates that the bonding of the antibody to the crosslinker injects additional electrons into the EG layers, further raising its Fermi level towards charge neutrality. Interestingly, following the cleaning process with NaCl solution to remove the antibody, the Raman spectra returned to that of the crosslinker/EG/SiC spectra due to the lack of covalent functionalization to the EG during processing, as shown in Fig S3(d), (i.e., the disappearance of both D peak and G peak redshift). The complete recovery of the redshift after the cleaning process with NaCl solution indicates that the charge transfer in this structure is fully recoverable and due to bonding interactions between the crosslinker and the antibody as opposed to bonding interactions between the EG and the antibody. The formation of a D peak in the spectra (Fig. S3(c)) would seem to indicate the formation of defects to the underlying graphene structure; however, the recovery of the D peak after the cleaning process with NaCl solution in order to remove the antibody indicates the formation of the D peak is due to the bonding interaction between the antibody and crosslinker (i.e., not damage to the underlying EG).

The cleaning process with NaCl solution also demonstrates the reusability of the crosslinker/EG/SiC structure, as the growth of the antibody does not induce damage in the underlying EG layer. In addition, all 2D peaks in the observed Raman spectra remained between 40-55cm$^{-1,}$ indicating that the bilayer character of the EG was maintained through all processing steps [1].
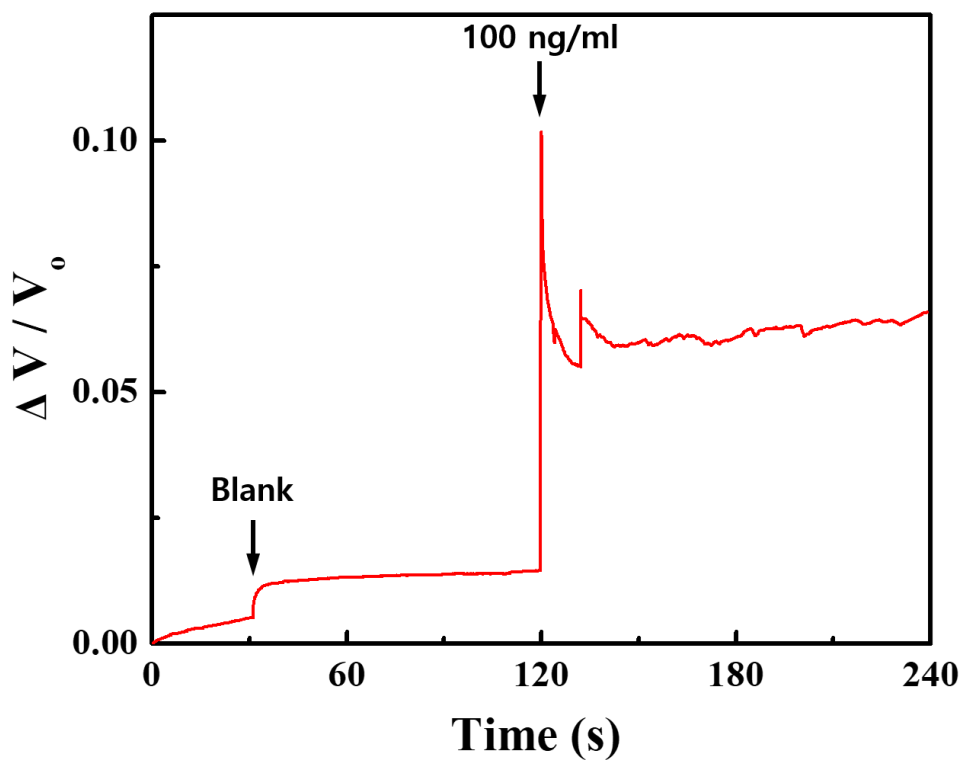
Figure S4 Real-time response of the SARS-CoV-2 S1 spike protein antigen on pure EG/SiC. Note that the spike protein was dissolved in ELISA assay diluent (1×) and dropped onto the sensor for the test. The pure EG/SiC-based sensor showed a response of 6.2 % with 100 ng/mL and that of 1.3 % with blank.
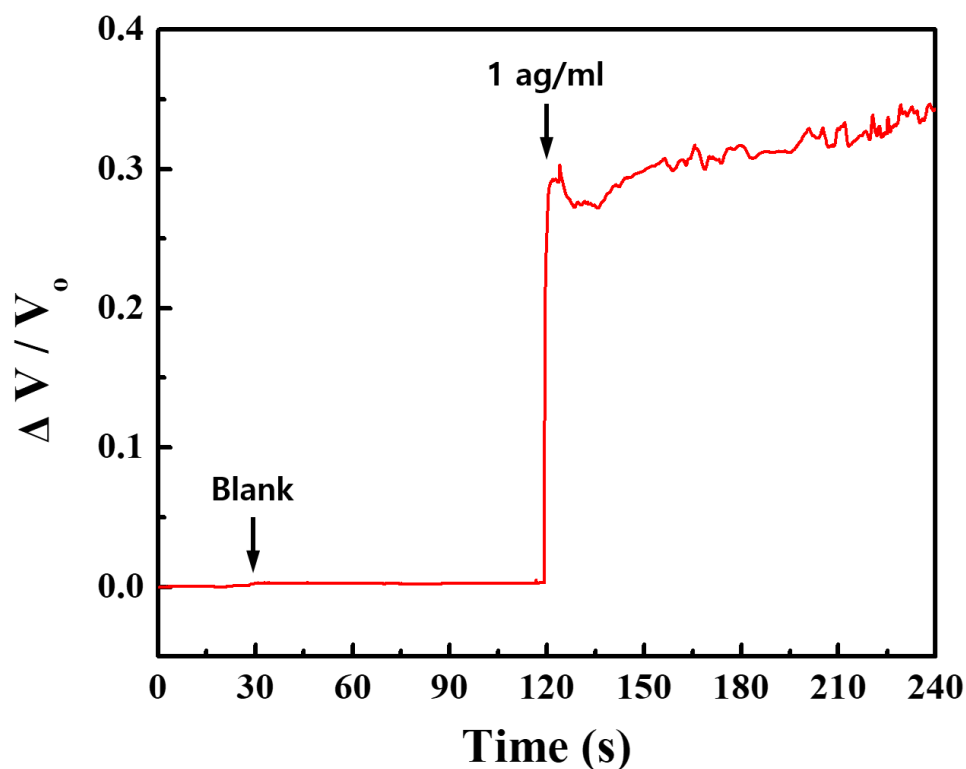
Figure S5 Real-time response of 1 ag/mL of the SARS-CoV-2 S1 spike protein (prepared by R&D SYSTEMS a biotechne brand) on the proposed sensor. The sensor clearly distinguished between blank and protein and showed a similar response result compared to the protein prepared by SinoBiological. The sensor had a signal-to-noise ratio of 68.66 dB and a response time of 1.5 s.
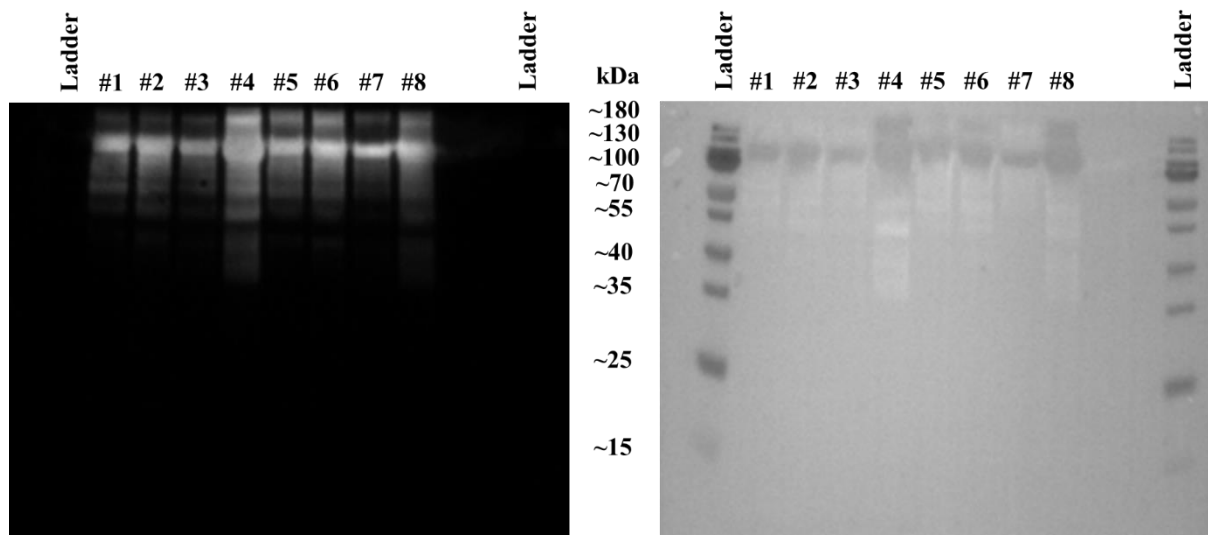
Figure S6 SDS-PAGE results of SARS-CoV-2 spike S1 protein. Protein extracts were prepared for SDS-PAGE using NuPAGE LDS sample loading buffer (Invitrogen). Prepared samples were separated on 12% NuPAGE gels in 1× MES buffer (Invitrogen) and transferred to PVDF membranes (Millipore). Blocked membranes were then incubated with 1:1000 primary antibody overnight, followed by washing and incubation with 1:10,000 secondary-HRP antibody. Signal was detected using the Supersignal West Pico Chemiluminescent substrate (Pierce) and imaged on the iBright imaging system with smart exposure (Invitrogen). Before the SDS-PAGE test, the proteins were deglycosylated (denaturing, non-denaturing) by PNGase F since the SARS-CoV-2 spike S1 protein is highly glycosylated.

Note: #1&5, 2&6: Sinobiological (same lot number), #3&7: R&D Systems (in PBS), #4&8: R&D Systems (in Water) #1-4: Denaturing, #5-6: Non-denaturing.
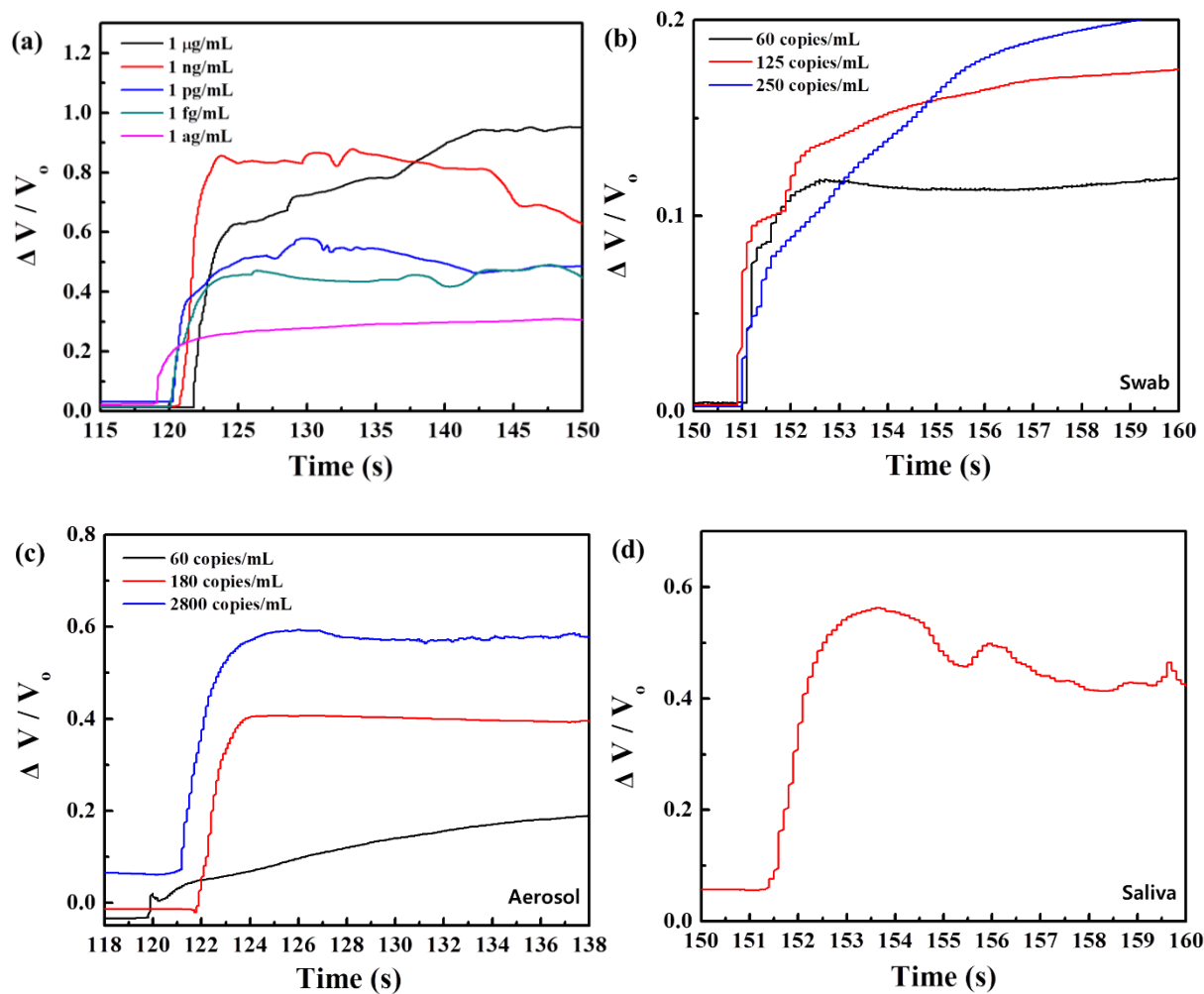
Figure S7 Magnified plot of the sensor output ($\Delta V/V_o$) to determine response times of (a) spike protein, (b) mid-turbinate swab, (c) exhaled breath aerosol, and (d) saliva samples.
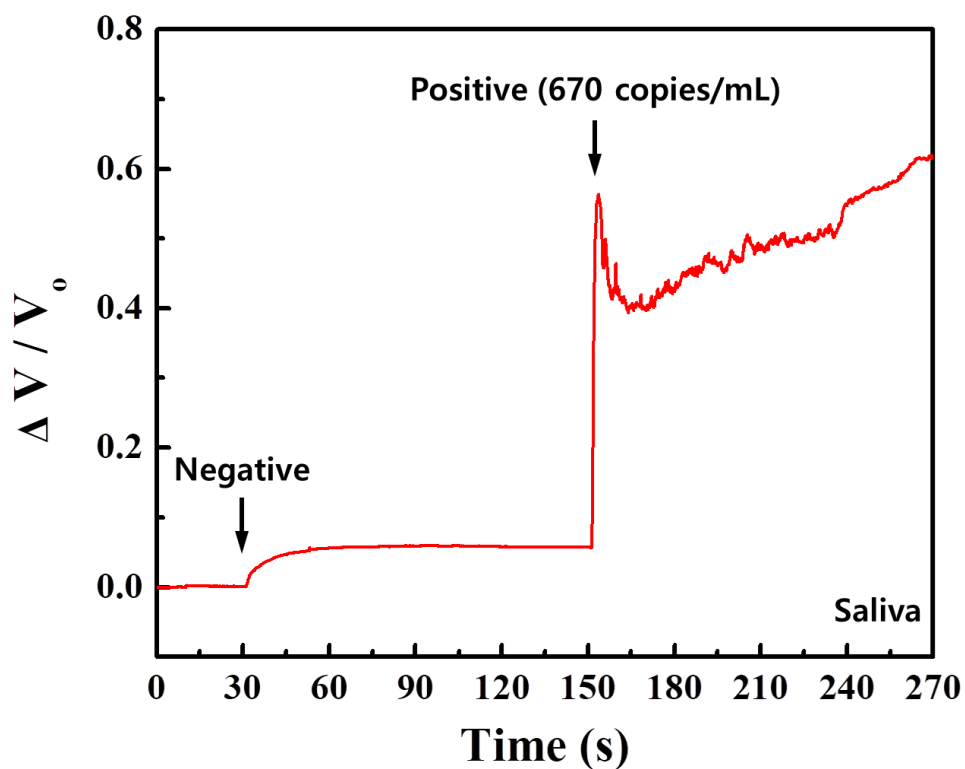
Figure S8 Detection performance of COVID-19 sensor using negative and positive human samples (patient #5: saliva, 670 copies/mL of SARS-CoV-2 virus) in real-time. Note that saliva samples were dissolved in 1% bovine serum albumin (BSA) in phosphate-buffered saline PBS) (1×), and 1 µL was dropped onto the sensor for the test. The sensor clearly distinguished between negative and positive samples and showed a signal-to-noise ratio of 39.2 dB and a response time of 1.1 s.

Portable COVID-19 sensor unit:

The portable unit has four main components: (1) a high frequency and sensitive galvanostat, (2) a microprocessor module, (3) a touchscreen interface and graphical user interface (GUI), and (4) a cloud storage link.

(1) High frequency and sensitive galvanostat

The most critical part of the system is the galvanostat. Because the entire concept depends on accurately measuring changes in resistance over time across our sensor, the galvanostat (which operates by adjusting a voltage across the sensor to maintain a constant current) must be able to track changes fast enough to measure the resistance correctly. It must also be able to do so at very low resistance changes since the concentration of virus particles on the sensor can vary widely. Thus we have developed a custom galvanostat module for this system that operates at 125 kHz, utilizes fA offset ultra-precision op-amps, along with a 16 bit DAC and 18 bit ADC to ensure enough sensitivity for measuring typical viral loads in clinical patient samples.

(2) Microprocessor module

The second part of the system is the microprocessor, which has three main functions: reading the voltage on the transimpedance amplifier (which is proportional to the current flowing through the sensor) and then controlling the DAC voltage across the sensor in order to maintain a constant current, saving this data to a file and then sending to a remote storage site via Wi-Fi, and using signal processing algorithms to determine whether a particular test run measured a positive result for SARS-CoV-2. The current portable unit uses a Linux application processor board.

(3) Touchscreen interface and graphical user interface (GUI)

The third part of the portable unit is the touchscreen interface and user GUI, which provides several important functions. First is a real-time plot of the current and voltage across the
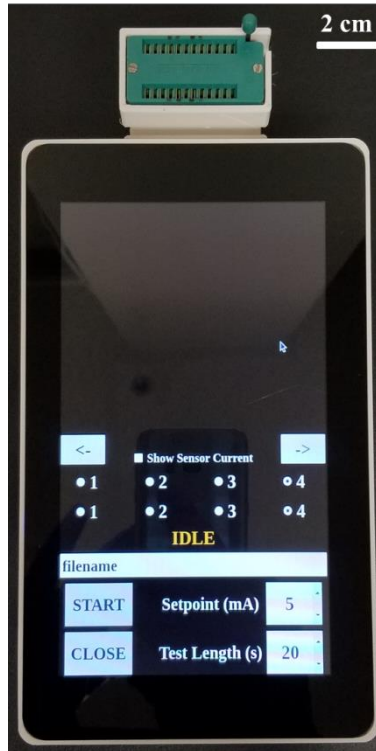
Figure S9 Photograph of the completed portable COVID-19 sensor unit. After initiating a test, the high-resolution galvanostat adjusts the voltage across the sensor until the desired setpoint current is measured to be flowing through it. It then maintains this current for the duration of the test. Once a sample (protein/virus) hits the proposed sensor, its resistance changes as the particles adhere to the surface and interact with the polyclonal antibodies. Again, the galvanostat adjusts to maintain the current. A signal processing algorithm is then used to determine the characteristics of the test and whether a positive result occurred. This data is then stored and sent over the internet to a cloud storage platform.

sensor (primarily for diagnostic use). Other options are setpoint current, test duration, and data filename. When a positive test is found, a new window appears to let the user know (Watch Supplementary Video 1).

(4) Cloud storage link

The last part of the portable unit is the cloud storage link. Because our device is battery-powered and fully portable, it utilizes Wi-Fi to send test results to a remote server. This will be critically important in situations where test results are automatically stored, such as at a hospital, school, or other high occupancy sites where regular testing is required (mass testing or mass vaccination sites, etc.)
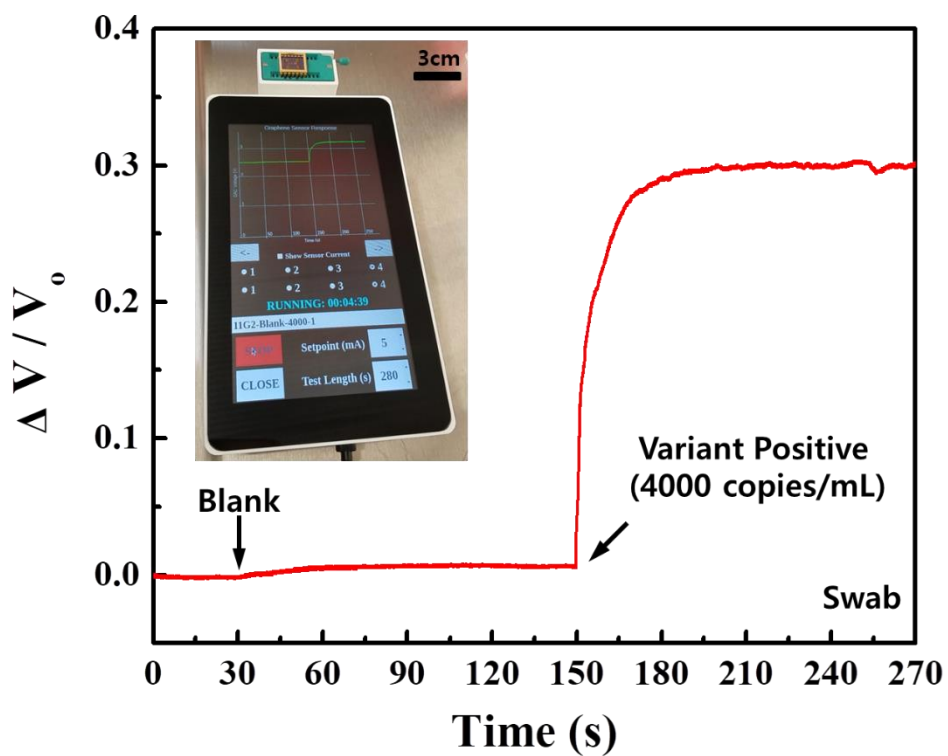
Figure S10 Demonstration of a practical diagnosis application of the proposed portable COVID-19 sensor testing positive human sample (patient #6: mid-turbinate swab, 4,000 copies/mL of B.1.1.7 variant) in real-time. The sensor clearly distinguished variant positive sample and showed a signal-to-noise ratio of 68.11 dB and a response time of 15 s.
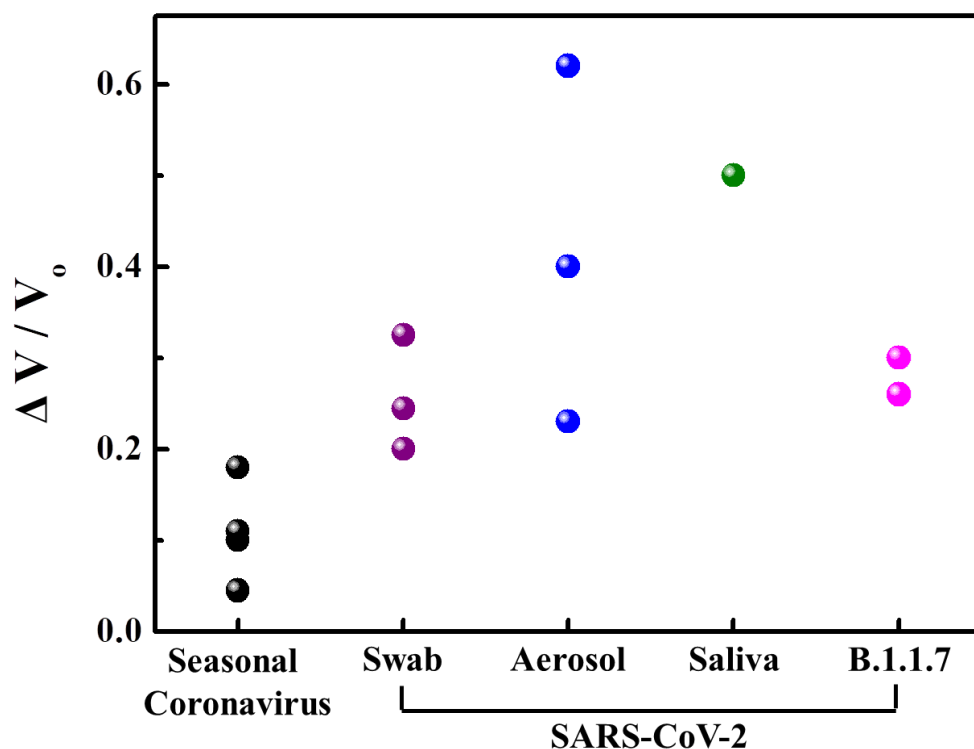
Figure S11 Graphical summary of the proposed sensors' responses with different samples such as seasonal coronaviruses (NL63, HKU1, NL63, and OC43), SARS-CoV-2 virus from infected patient samples (mid-turbinate swabs, saliva, exhaled breath aerosol, and B.1.1.7 variant). The proposed sensors' response shows at least 20% changes when exposed to SARS-CoV-2 with 60 copies/mL (i.e., LOD of the sensor), while the response for the seasonal coronaviruses with ~10^8 copies/mL changes up to 18%.

Note: Swabs (60, 125, and 250 copies/mL), Aerosol (60, 180, and 2800 copies/mL), Saliva (670 copies/mL), B.1.1.7 variant (swab: 4000 copies/mL, saliva: 8000 copies/mL).
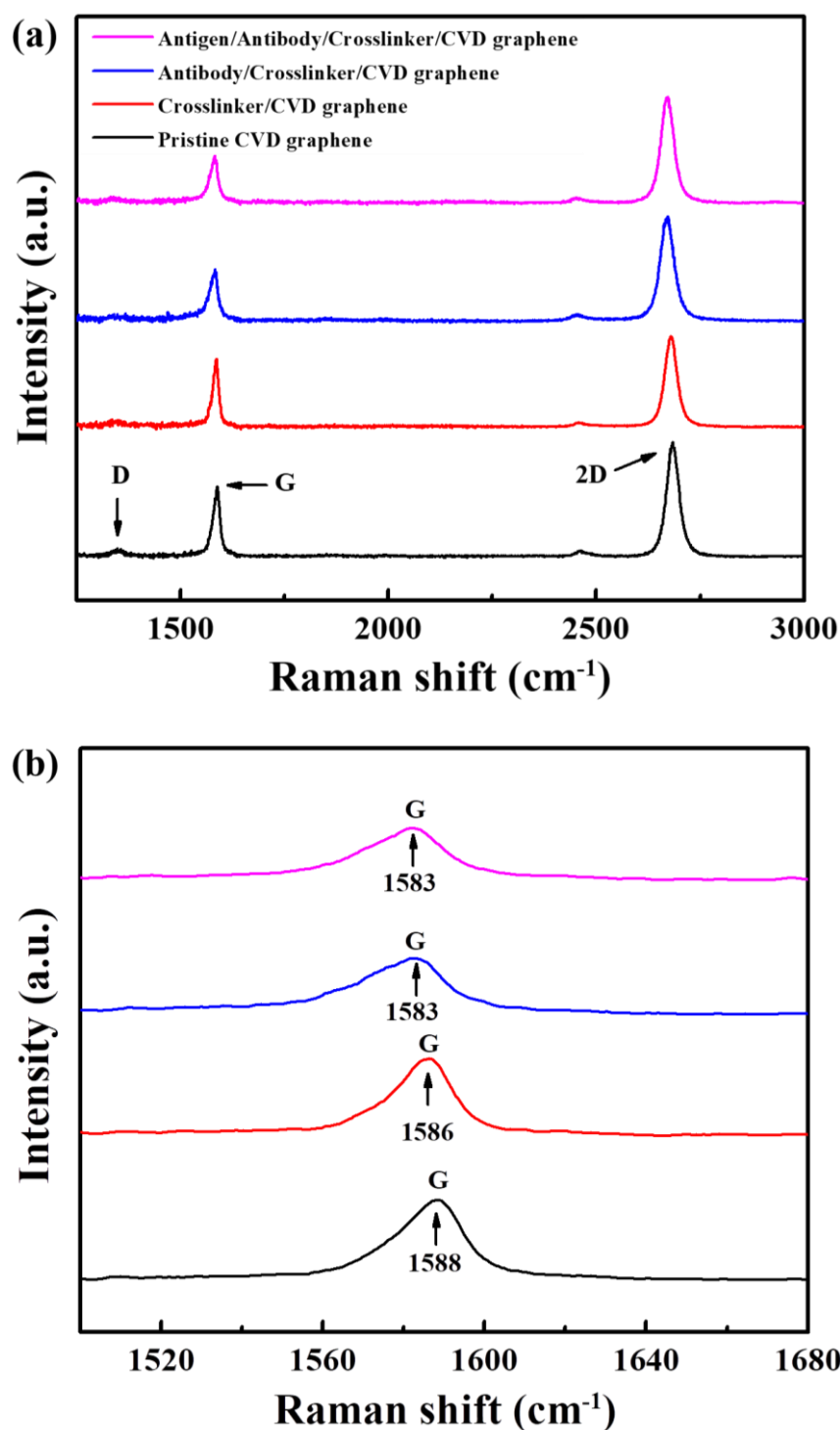
Figure S12 (a) Raman spectra of CVD graphene with different layers such as crosslinker, SARS-CoV-2 spike S1 protein antibody, and antigen (1 ag/mL). The CVD graphene was transferred to the SiO_2/Si substrate before the immobilization. The pristine CVD graphene shows typical Raman results of monolayer graphene. (b) A magnified plot of the Raman spectra to investigate the graphene G peak position with each layer. The Raman spectra of the crosslinker prepared on CVD graphene show a 2 cm^{-1} redshift of the G peak compared to its pristine graphene, while that of the antibody/crosslinker/graphene displays an additional 3 cm^{-1} redshift of the G peak. However, there is no further shift of G peak with SARS-CoV-2 spike S1 protein antigen (1 ag/mL), unlike our proposed sensor with EG shows an additional 2 cm^{-1} redshift of the G peak.

Table S1. Clinical characteristics of patients (mid-turbinate swabs, saliva, and exhaled breath aerosol samples) with COVID-19.

	Patient #1	Patient #2	Patient #3	Patient #4	Patient #5	Patient #6
# of copies per mL	313,000 (original) 60 – 250 (diluted)	60	180	2,800	670	1,990,000 (original, swab) 13,100,000 (original, saliva) 4000 – 8000 (diluted)
Oral temperature (°F)	99.5	99	98.6	99.1	99.1	99
Runny nose	1	1	1	1	1	1
Stuffy nose	2	1	1	2	1	0
Sneeze	2	1	1	0	1	0
Sore throat	0	1	0	1	0	0
Earache	0	0	0	1	0	0
Malaise (tiredness/ fatigue)	2	1	2	2	2	1
Headache	2	1	3	3	1	1
Muscle/joint ache	0	1	1	2	0	1
Sweats/fever/chills	0	1	0	1	0	0
nausea	0	0	0	1	0	0
Loss of appetite	1	0	1	1	0	0
Vomit	0	0	0	0	0	0
Diarrhea	0	0	0	0	0	0
Chest tightness	2	0	0	0	0	0
Shortness of breath	0	0	0	1	0	0
Cough	1	0	0	1	0	2
Loss of taste/smell	1	0	0	1	0	0

*The numbers indicate how severe the patients felt for each symptom.
No pain=0; Mild=1; Moderate=2; Severe=3

Table S2. Comparison of the performance of SARS-CoV-2 detection with various technology

Technology/ Materials	Sample (validation)	Sample preparation step	Response time	Limit of detection (copies/mL)	Portability
Epitaxial graphene [This work]	Mid-turbinate swabs, saliva, exhaled breath aerosol, spike protein	X	0.6 s – 32 s	1 ag/mL 60 copies/mL	O
Immunoassay [Ref. 8]	Sputum	X	< 10 min	100 copies/mL	O
PCR [Ref. 9]	Sputum	O (1.5 h)	< 3 h	83.1 copies/mL	X
PCR [Ref. 10]	Viral RNA	O (1.5 h)	< 3 h	15 copies/mL	X
LAMP [Ref. 11]	Standard RNA	O (1.5 h)	< 1.5 h	100 copies/mL	X
Graphene based FET [Ref. 12]	Nasopharyngeal swab	X	> 1 min	242 copies/mL	-
SENSR [Ref. 13]	Viral RNA, Nasopharyngeal swab	X	< 30 min	60 copies/mL	O
RT-LAMP [Ref. 14]	Viral RNA	X	< 30 min	50 copies/μL	O
CRISPR-Cas13a [Ref. 15]	Viral RNA, Nasopharyngeal swab	X	< 30 min	100 copies/μL	O
Co-functionalized TiO$_2$ nanotubes [Ref. 16]	Spike protein	X	> 1 min	14 nM	-
Graphene [Ref. 17]	Saliva, Blood	X	< 10 min	500 pg/mL (NP)	O

References

[1] K.M. Daniels, M.M. Jadidi, A.B. Sushkov, A. Nath, A.K. Boyd, K. Sridhara, H.D. Drew, T.E. Murphy, R.L. Myers-Ward, D.K. Gaskill, *2D Mater.* **2017, 4**, 025034.

[2] W. Xie, L.T. Weng, K.M. Ng, C.K. Chan, C.-M. Chan, *Carbon*, **2017**, *112*, 192-200.

[3] R. Al-Gaashani, A. Najjar, Y. Zakaria, S. Mansour, M.A. Atieh, *Ceramics Int.* **2019, *45*,** 14439-14448.

[4] C.-M. Chen, Q. Zhang, X.-C. Zhao, B. Zhang, Q.-Q. Kong, M.-G. Yang, Q.-H. Yang, M.-Z. Wang, Y.-G. Yang, R. Schologl, D.S. Su, *J. Mat. Chem*, **2012**, *22*, 14076-14084.

[5] Z. Luo, T. Yu, Z. Ni, S. Lim, H. Hu, J. Shang, L. Liu, Z. Shen, J. Lin, *J. Phys. Chem.* **2011**, *115*, 1422-1427.

[6] Z.H. Ni, T. Yu, Z.Q. Luo, Y.Y. Wang, L. Liu, C.P. Wong, J. Miao, W. Huang, Z.X. Shen, *ACS Nano* **2009**, *3*, 569-574.

[7] S. Kim, Y. Dong, M.M. Hossain, S. Gorman, I. Towfeeq, D. Gajula, A. Childress, A.M. Rao, G. Koley, *ACS Appl. Mater. Interfaces* **2019**, *11*, 16006-16017.

[8] B. Giri, S. Pandey, R. Shrestha, K. Pokharel, F. Ligler, B.B. Neupane, *Anal. Bioanal. Chem.* **2021**, *413*, 35-48.

[9] D.K.W. Chu, Y. Pan, S.M.S. Cheng, K.P.Y. Hui, P. Krishnan, Y. Liu, D.Y.M. Ng, C.K.C. Wan, P. Yang, Q. Wang, M. Peiris, L.L.M. Poon, *Clin. Chem.* **2020**, *66*, 549-555.

[10] Y. Jung, G.-S. Park, J.H. Moon, K. Ku, S.-H. Beak, C.-S. Lee, S. Kim, E.C. Park, D. Park, J.-H. Lee, C.W. Byeon, J.J. Lee, J.-S. Maeng, S.-J. Kim, S.I. Kim, B.-T. Kim, M.J. Lee, H.G. Kim, *ACS Infect. Dis.* **2020**, *6*, 2513-2523.

[11] G.-S. Park, K. Ku, S.-H. Baek, S.-J. Kim, S.I. Kim, B.-T. Kim, J.-S. Maeng, *J. Mol. Diagn.* **2020**, *22*, 729-735.

[12] G. Seo, G. Lee, M.J. Kim, S.-H. Baek, M. Choi, K.B. Ku, C.-S. Lee, S. Jun, D. Park, H.G. Kim, S.-J. Kim, J.-O. Lee, B.T. Kim, E.C. Park, S.I. Kim, *ACS Nano* **2020**, *14*, 5135-5142.

[13] C.H. Woo, S. Jang, G. Shin, G.Y. Jung, J.W. Lee, *Nat Biomed. Eng.* **2020**, *4*, 1168-1179.

[14] A. Ganguli, A. Mostafa, J. Berger, M.Y. Aydin, F. Sun, S.A. Stewart de Ramirez, E. Valera, B.T. Cunningham, W.P. King, R. Bashir, *PNAS* **2020**, *117*, 22727-22735.

[15] P. Fozouni, S. Son, M. Diaz de Leon Derby, G.J. Knott, C.N. Gray, M.V. D'Ambrosio, C. Zhao, N.A. Switz, G.R. Kumar, S.I. Stephens, D. Boehm, C.-L. Tsou, J. Shu, A. Bhuiya, M. Armstrong, A.R. Harris, P.-Y. Chen, J.M. Osterloh, A. Meyer-Franke, B. Joehnk, K. Walcott, A. Sil, C. Langelier, K.S. Pollard, E.D. Crawford, A.S. Puschnik, M. Phelps, A. Kistler, J.L. DeRisi, J.A. Doudna, D.A. Fletcher, M. Ott, *Cell* **2021**, *184*, 323-333.

[16] B.S. Vadlamani, T. Uppal, S.C. Verma, M. Misra, *Sensors* **2020**, *20*, 5871.

[17] R.M. Torrente-Rodriguez, H. Lukas, J. Tu, J. Min, Y. Yang, C. Xu, H.B. Rossiter, W. Gao, *Matter* **2020**, *3*, 1981-1998.